Shock initiation and propagation of detonation in ANFO

Bohanek, Vječislav; Štimac Tumara, Barbara; Serene, Chan Hay Yee; Sućeska, Muhamed

MDPI

Article

Shock Initiation and Propagation of Detonation in ANFO

Vječislav Bohanek [1,*], Barbara Štimac Tumara [1], Chan Hay Yee Serene [2] and Muhamed Sućeska [1]

1 Department of Mining Engineering and Geotechnics, Faculty of Mining, Geology and Petroleum Engineering, University of Zagreb, Pierottijeva 6, 10000 Zagreb, Croatia

2 Emerging Nanoscience Research Institute, Nanyang Technological University, 50 Nanyang Avenue, North Spine, Block N1-B4a-02, Singapore 639798, Singapore

* Correspondence: vjecislav.bohanek@rgn.unizg.hr

Abstract: The ammonium nitrate (AN) and fuel oil (FO) mixture known as ANFO is a typical representative of non-ideal explosives. In contrast to ideal explosives, the detonation behavior of ANFO exhibits a strong dependence on charge diameter, existence, and properties of confinement, with a large failure diameter and long distance required to establish steady-state detonation. In this study shock initiation and propagation of detonation in ANFO were studied experimentally by determining the detonation velocity at different distances from the initiation point, as well as by numerical modeling using AUTODYN hydrodynamics code and a Wood–Kirkwood detonation model incorporated into EXPLO5 thermochemical code. The run-to-steady-state detonation velocity distance was determined as a function of charge diameter, booster charge mass, and confinement. It was demonstrated that a Lee–Tarver ignition and growth reactive flow model with properly calibrated rate constants was capable of correctly ascertaining experimentally observed shock initiation behavior and propagation of detonation in ANFO, as well as the effects of charge diameter, booster mass, and confinement.

Keywords: ANFO; shock initiation; detonation; numerical modeling; EXPLO5; AUTODYN

1. Introduction

Ammonium nitrate (AN)-based explosives have been attractive candidates as blasting agents in the mining industry due to their low production cost and relatively simple production processes. High porosity, low density, and separated fuel (FO) and oxidizing agents (AN) differentiate ANFO from conventional high explosives, where the fuel and oxidizer are in a single molecule and typically display "ideal" behavior. ANFO is a typical "non-ideal" explosive, and its detonation properties exhibit a strong dependence on charge diameter, existence, and properties of confinement [1–3].

Depending on various factors, such as the type of AN, density, charge diameter, and confinement, the detonation velocity (VoD) might go as low as 40% of the ideal detonation velocity [4]. Velocities between 1.2 and 3.0 km/s were reported by [5] with fine granular AN, paper tube confinement, and diameters in the range of 127–460 mm, while velocities up to 3.5 km/s were reported by [6] with prilled AN. The authors of [7] and [8] reported the calculated ideal detonation velocity of ANFO to be 4.94 km/s (at $\rho_0 = 0.88$ g/cm^3) and 4.79 km/s (at $\rho_0 = 0.8$ g/cm^3), respectively.

Despite its non-ideal detonation characteristics, its significant amount of gaseous detonation products results in a substantial destructive power, making ANFO one of the most widely used blast explosives.

The effects of different variables on the detonation performance of ANFO have been well-researched and published. The main variables include [9] the fuel/oil ratio, the properties of the AN prills [10–12], and the density and charge diameter [7]. Other variables affecting VoD, such as the initiating energy [13], the charge temperature [14], the presence of additives [15], and the influence of confinement [16,17], have been reported on as well. Using underwater initiation capability tests, ref. [13] determined the influence of initiation

energy, equivalent shock energy, and bubble energy on the VoD. They found that the velocity of detonation increased with the increasing mass of the PETN booster charge (up to 3.5 km/s) compared to reference detonators (up to 2.5 km/s). Further, using primers of different densities, weights, and VoDs, ref. [9] found that the type of primer influenced the measured detonation velocity of ANFO, increasing from 3.28 km/s to 3.56 km/s when using different primers.

The heterogenous nature of ANFO complicates the shock initiation process, as initiation depends on the shock wave duration and strength, as well as on the mechanisms of grain burning and hot spot formation [2]. Numerical modeling of the shock initiation of ANFO has been greatly aided by the extensive research and VoD data reported on ANFO. Because of its wide reaction zone and curved shock front, the development of non-ideal detonation models is challenging and has lagged behind ideal detonation models, such as the Chapman–Jouguet (CJ) model, which assumes instantaneous reaction with no reaction zone width. The ideal detonation velocity of ANFO explosives calculated by several thermochemical codes using different equations of state (EOSs) was compared by [18]. Unfortunately, most of those codes are based on ideal CJ theory and do not adequately describe the non-ideal detonation behavior of ANFO and much less realistically demonstrate the effects of test parameters. The thermochemical equilibrium code EXPLO5 [19] offers a kinetic module based on Wood and Kirkwood's (WK) detonation theory [2,20,21], which enables the calculation of detonation properties of non-ideal explosives.

In this work, we study detonation initiation and propagation in ANFO charges (a) experimentally by determining the detonation velocity as a function of distance from the initiation point, as well as (b) by numerical modeling. A two-pronged computational strategy is applied: the WK model is incorporated into EXPLO5 for calculation of the steady-state detonation velocity of unconfined charges, and the AUTODYN hydrodynamics code is used to model both the initiation and propagation of detonation as a function of charge diameter, the existence of confinement, and the booster mass. The objective of the work is to examine whether it is possible for reactive flow models to correctly describe and predict the shock initiation and detonation behavior of ANFO charges.

2. Description of Numerical Models

2.1. Shock Initiation Modeling with AUTODYN

The Lee–Tarver ignition and growth (I&G) model [22] has been implemented in many hydrodynamics codes, such as AUTODYN, and is perhaps the most widely used reactive model for studying shock initiation in explosives. The I&G model comprises two Jones–Wilkins–Lee (JWL) EOSs: one for the unreacted explosive and the other for the reaction products. The conversion from unreacted explosive to reacted explosive (i.e., detonation products) is controlled by a two-term pressure-dependent reaction rate given by the following equation [22]:

$$\frac{\partial F}{\partial t} = I(1-F)^b(\mu-a)^x + G(1-F)^c F^d p^y \tag{1}$$

where F is the reacted fraction (or conversion); p is the pressure; $\mu = (\rho/\rho_0 - 1)$ is the compression; and I, a, b, c, d, x, y, and G are constants.

The I&G model assumes that ignition starts at hot spots and growth extends outwards. The first term in Equation (1) is related to the formation of hot spots upon the action of a shock wave, and the second term corresponds to the growth of the reaction. The first term is set to zero after a certain conversion (F_{Igmax}) is reached, after which the growth term is switched on. The initial reaction rate parameters in our model were inspired by [23], who proposed rate constants that have a physical basis (e.g., compression exponent $x = 4$ approximates the amount of plastic work required for dynamic void collapse; pressure exponent $y = 0.9$ describes weak, pressure-dependent laminar burning; etc.). Thus, in our study we used values of constants from [22] (I, a, b, c, d, x, and y) and adjusted only the

constant G to reproduce our experimental steady-state detonation velocity charge diameter data (Table 1).

Table 1. Input parameters for reacted and unreacted ANFO with an initial density 0.8 g/cm^3.

Reacted ANFO [a]	Unreacted ANFO [b]	Lee–Tarver I&G Reaction Rate Parameters [c]
A = 81.6492 GPa	A = 1454.25 GPa	I = 10 1/μs
B = 1.7537 GPa	B = −0.347 GPa	a = 0.2
R_1 = 4.588863	R_1 = 21.8866	b = 0.222
R_2 = 1.021101	R_2 = 0.7874	x = 4
ω = 0.32021	ω = 3.4613	G = 0.086 1/(μs GPa $^{\wedge}$y)
D = 4.78 km/s	E_0 = −0.1549 kJ/cm^3	c = 0.222
p_{CJ} = 4.61 GPa		d = 0.666
E_0 = 3.4481 kJ/cm^3		y = 0.9
		F_{Igmax} = 0.3

Legend: [a] calculated by EXPLO5; [b] derived from Murnaghan EOS data; [c] all parameters except G are taken from [23], and G is adjusted to reproduce our experimental VoD data.

The JWL EOS was used for unreacted ANFO, detonation products, and the PETN booster explosive. The JWL EOS had the following form [22]:

$$p = A\left(1 - \frac{\omega}{R_1 V}\right)e^{-R_1 V} + B\left(1 - \frac{\omega}{R_2 V}\right)e^{-R_2 V} + \frac{\omega E}{V} \tag{2}$$

where V is the relative volume (V/V_0); E is the detonation energy; and A, B, R_1, R_2, and ω are constants.

The JWL parameters for ANFO's detonation products were derived from EXPLO5 calculations, as described in [24]. The JWL parameters for unreacted ANFO were derived in the following way. First, the Murnaghan EOS given by [25] was used:

$$p = \frac{1}{n\kappa}\left(\frac{1}{V^n} - 1\right) \tag{3}$$

where $n = (4S_1 - 1)$, and $\kappa = 1/\rho_0 C_0^2$ is used to generate p-V data along the shock adiabat of unreacted ANFO. Then, the so-obtained p-V data were fitted to the JWL EOS to derive the JWL constants. The values of S_1 and C_0 for ANFO were taken from [26] and given by C_0 = 0.92 km/s and S_1 = 1.4. for a density of 0.8 g/cm^3.

The JWL parameters for the PETN booster (1.5 g/cm^3 density) were taken from the built-in material library in AUTODYN [27]. The PVC confinement was modeled with Shock EOS, whereby the EOS parameters for PVC were taken from the work of [28]. Steel confinement was modeled assuming the material properties of 4340 alloy steel taken from the AUTODYN material library [27]. The dynamic behavior of steel was modeled using the Johnson–Cook failure model, the Johnson–Cook strength model, and Shock EOS [27,29].

The numerical simulation was carried out using a 2D axisymmetric Lagrangian formulation. The element size (axial × radial) for both the explosive and confinement was 1 × 1 mm for all the calculations. Lightly PVC-confined ANFO charges were initiated using a cylindrical PETN booster charge of constant mass (20 g, d = 20 mm, and ρ_0 = 1.5 g/cm^3), while steel-confined ANFO charges were initiated by PETN boosters of different masses, with an equivalent booster diameter-to-length ratio of 1. The point of initiation was set at the front end of the booster charge. Gauges were placed at regular intervals within the explosive charge (50 mm on the first third of the charge and 100 mm after that) to register the time of arrival of the detonation wave to determine the shock velocity.

2.2. Calculation of Steady-State Detonation Applying Wood–Kirkwood Detonation Model

The steady-state detonation velocity of ANFO was calculated by applying the Wood–Kirkwood (WK) detonation theory incorporated into EXPLO5 thermochemical code [19,24]. The WK theory predicts detonation velocity as a function of charge radius and considers the radial expansion of detonation products. The hydrodynamic variables and chemi-

cal concentrations of reactant and products along the center of the cylinder are given as a set of ordinary differential equations and are supplemented by the reaction rate, the rate of radial expansion, and equations of state of the detonation products and unreacted ANFO [20,30]. The state of gaseous detonation products can be described by the Becker–Kistiakowsky–Wilson EOS [31], and that of condensed detonation products by the Murnaghan EOS [26,32,33]. The parameters for both EOSs were taken from the EXPLO5 library [19].

The state of unreacted ANFO is described by the Murnaghan EOS (Equation (3)). The parameters in the Murnaghan EOS for unreacted ANFO with a density 0.8 g/cm^3 were taken from [26]: C_0 = 0.92 km/s and S_1 = 1.4.

To describe the rate of radial expansion (ω_r) of the detonation products, we used Wood and Kirkwood's [20] radial expansion model, which relates the rate of radial expansion and the shock front curvature radius:

$$\omega_r = \frac{(D-u)}{R_C} \tag{4}$$

where R_c is the shock front curvature radius, u is the particle velocity in the shock frame, and D is the detonation velocity.

The shock front curvature radius was calculated using the dependence proposed by [34]:

$$R_C = aR_0^b \text{ (in mm)} \tag{5}$$

where R_0 is the charge radius, a = 0.4256, and b = 1.3835.

The reaction rate was described by two rate models: a two-step I&G rate model (Equation (1)) and a single-step pressure-based (PB) reaction rate model [8,35]:

$$\frac{dF}{dt} = k(1-F){\cdot}P^D \tag{6}$$

where k and D are rate constants.

The constants k and D were calibrated to reproduce our experimental VoD charge radius data for ANFO and were found to be k = 0.0471/µs and D = 1.4. The rate constants for the I&G model were the same as those used in AUTODYN (Table 1), except for G, which was tuned to better reproduce both experimental VoD charge radius data and the width of the detonation driving zone, equaling G = 0.041/(µs p$^{0.9}$).

3. Results and Discussion

3.1. Materials and Methods

The study was conducted with commercially available ANFO explosive containing 94.6% AN and 5.4% fuel oil, with a minimal oil absorption of 6% and AN prill sizes ranging between 1.0 and 2.83 mm. The density of the ANFO charges was in the range of 0.78–0.82 g/cm^3.

The velocity of detonation of cylindrical ANFO charges was measured by an electro-optical method using a six-channel Kontinitro EXPLOMET-FO-2000 detonating velocity measuring system [24]. Optical fibers were placed along the charge axis at even distances, with the first sensor at a minimum of 50 mm from the initiation point. The detonation velocity was determined by measuring the time of arrival at 5 different positions (sections) along the charge axis, as illustrated in Figure 1. The distance between the fibers was 120 mm for charges with inner diameters of 71 and 154 mm and 150 mm for other charges. The values of the detonation velocities at the middles of sections were used for analysis.

Two sets of measurements were performed: the first using lightly confined ANFO charges (thin polyvinyl chloride confinement, PVC) to determine the effect of charge diameter on detonation velocity–distance profiles and the second using ANFO charges confined in 3 mm thick steel tubes to determine the effects of confinement and booster mass on detonation velocity–distance profiles.

In the first set of measurements, the inner charge diameters varied from 71 mm to 154 mm, with lengths from 700 to 1000 mm and PVC tube thickness of 2–3 mm. The initiation was kept the same throughout the set with the use of an instantaneous electric detonator and 20 g of PETN booster. In the second set of measurements, the inner diameter of the ANFO charges was 55 mm and the length 500 mm. The initiation was performed using cylindrical PETN boosters of different masses (1 g, 20 g, 50 g, and 100 g) while keeping the booster length-to-diameter ratio constant at 1. The detonation velocity was measured at four sections along the charge axis. The distance between the fibers was 100 mm. For the first set of experiments, two tests were performed for each charge diameter and the mean value of detonation velocity was taken, and for second set, three tests were performed. In both sets of measurements, the average density of the explosive charges was 0.8 g/cm^3.
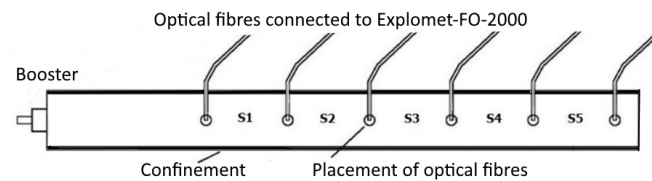

Figure 1. Schematic representation of measuring system.

3.2. Effect of Charge Diameter on Shock Initiation Behavior

The effect of charge diameter on the shock initiation and propagation of detonation in ANFO was studied experimentally using lightly confined charges having internal diameters of 71 mm, 104 mm, 119 mm, and 154 mm. Detonation velocity was measured at five sections at different distances from the initiation point. The so-obtained detonation velocities are shown in Figure 2 as a function of distance from the booster back end.
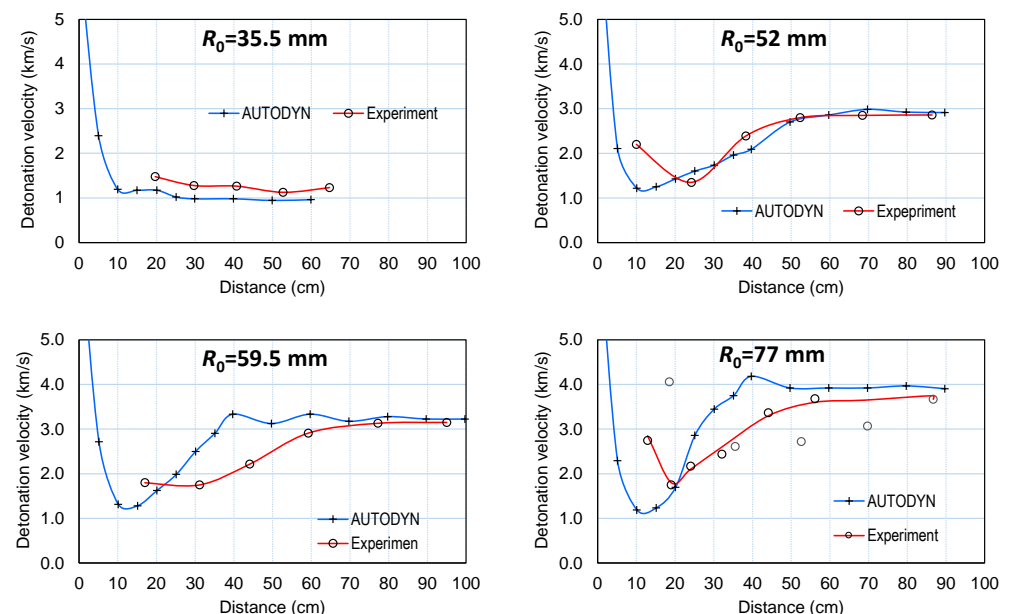

Figure 2. Experimental and calculated detonation velocities of slightly confined ANFO charges having different radii as a function of distance from the booster.

Numerical modeling with AUTODYN was performed as described in Section 2.2. Detonation velocities at individual sections of the charge were calculated from the registered time of arrival of the shock front to individual gauges located along the charge axis and the distance of the gauges from the initiation point. The arrival time was determined from the pressure–time curve (Figure 3) for each gauge. The calculated detonation velocities for the 71 mm, 104 mm, 119 mm, and 154 mm charge diameters are shown in Figure 2, along with experimentally obtained data. The density of the charges was 0.8 g/cm^3.

As is visible in Figure 2, both experiments and calculation showed a sharp drop in VoD after shock waves entered the ANFO charges, reaching a VoD minimum value of about 1.2 km/s after approximately 100–120 mm (from AUTODYN calculations) and after 200–300 mm (from experiments). After that, the VoD increased and achieved steady-state velocity for a given charge diameter. The run-to-steady-state detonation velocity distance (x_{SDT}) decreased with increase in the charge diameter and ranged between 500 and 700 mm, i.e., 3–6 charge diameters (Table 2).
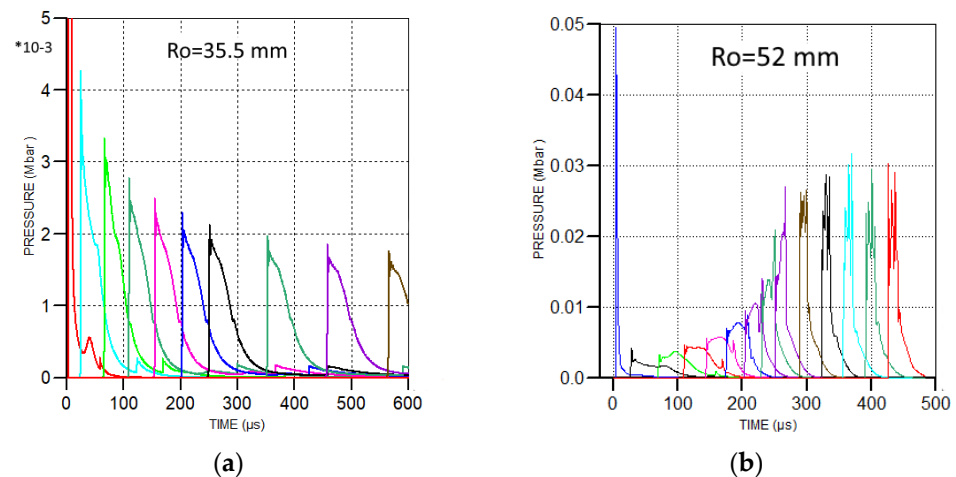

(**a**)　　　　　　　　　　　　　　　　　　　　(**b**)

Figure 3. Calculated pressure–time profiles along the charge axis for (**a**) 35.5 mm and (**b**) 52 mm charge radii.

Table 2. Experimental and calculated detonation velocities and run-to-steady-state detonation velocity distances at different charge radii.

d_{in} (mm)	R_0 (mm)	Detonation Velocity (km/s)				x_{SDT} (mm)		x_{SDT}/d_{in}
		Expt.	AUTODYN (at $x > x_{SDT}$)	EXPLO5 (PB Model)	EXPLO5 (I&G Model)	Expt.	AUTODYN	
71	35.5	1.23	0.96	-	-	-	-	
90	45		1.63	2.48	2.34		1000 *	11.11
98	49		2.69	2.78	2.61		720	7.35
104	52	2.85	2.88	2.94	2.77	600	600	5.77
119	59.5	3.15	3.31	3.22	3.10	650	420	3.53
154	77	3.68	3.89	3.58	3.57	500	380	2.47
250	125		4.59	4.01	4.10		300	1.20
1000	500		4.85	4.56	4.57		280	0.28

Legend: Expt.—experimental data; *—approximated.

When comparing the experimental and calculated VoD–x curves for the four studied charge diameters, one can note that the calculated steady-state detonation velocities agreed very well with the experimental velocities (Table 2). For example, for the 77 mm charge radius, AUTODYN predicted a detonation velocity of 3.89 km/s, while EXPLO5 with the I&G reaction rate model predicted 3.57 km/s, which were 5.7% higher and 2.9% lower than the experimental detonation velocity of 3.68 km/s, respectively.

The calculated and experimental VoD–x profiles were in good qualitative agreement. However, the values of the VoD at minimum and the run-to-steady-state detonation distance were somewhat different. For example, the calculated minimum VoD was achieved earlier (after 100–120 mm) compared to the experimental minimum (200–300 mm), and its value was higher than the experimental value (1.7 km/s versus 1.2 km/s). In addition, a faster growth in VoD from the minimum value to a steady-state velocity, i.e., a shorter x_{SDT}, was predicted by the calculations.

The difference between the calculations and experiments may be attributed partly to the shortcomings of the experimental set-up and partly to the inadequacies of the numerical

model. From the experiments, the measurement of VoD on five sections along the charge axis may be insufficient to obtain a smooth and accurate VoD–x profile, particularly in the region closer to the initiation point where abrupt change in VoD was observed. As for the numerical model, the calculated VoD–x profiles resulted from the combined effect of chemical and mechanical responses, which implies that both the equations of state of unreacted ANFO and the reaction rate model were imperative to obtain an accurate depiction of the detonation behavior. Since in our model reaction rate constants were calibrated to reproduce experimental steady-state detonation velocity, inaccuracy of the unreacted EOS seems to be the more likely cause of discrepancy between the experimental and modeling results rather than the reaction rate model.

The VoD–x profiles shown in Figure 1 are characteristic of shock initiation in heterogeneous explosives. The shock wave generated by the booster charge propagated into the main ANFO charge, and its intensity attenuated quickly with distance. At the same time, some of the reaction occurred just behind the shock front (hotspot reaction), causing pressure growth. Most of the reaction occurred behind the leading shock (growth in reaction), generating a pressure wave that overtook the initial shock wave and caused the process to finally transition to steady-state detonation [36]. This is clearly seen in Figure 3, which shows calculated pressure–time profiles along the charge axis.

Figure 3b shows that pressure generated by the booster charge dropped quickly to approximately 0.3 GPa (0.003 Mbar) in less than 80 μs. The same applied for the 59.5 mm and 77 mm charges. When the reaction rate became significant, pressure accelerated quickly to a pressure that corresponded to steady-state detonation. The pressure growth was clearly visible for the 52 mm, 59.5 mm, and 77 mm charge radii. However, for $R_0 = 35.5$ mm (Figure 3a), pressure continuously and slowly decreased, approaching about 0.18 GPa (resulting in VoD = 0.96 km/s) at $x = 550$ mm. This indicates that steady-state detonation velocity was not achieved after 550 mm. Such an effect of charge diameter on the shock initiation behavior of ANFO resulted from larger radial expansion of the detonation products and, consequently, larger pressure weakening in the case of smaller charge diameters. The final shape of the VoD–x curves was determined by an interplay between the rate of expansion of the detonation products and the rate of reaction for a given charge size. To obtain clearer insight into the dependence of initiation behavior on charge diameter, several calculations were carried out for charge diameters ranging from 71 to 1000 mm. The results of the calculations are shown in Figure 4 and Table 2.
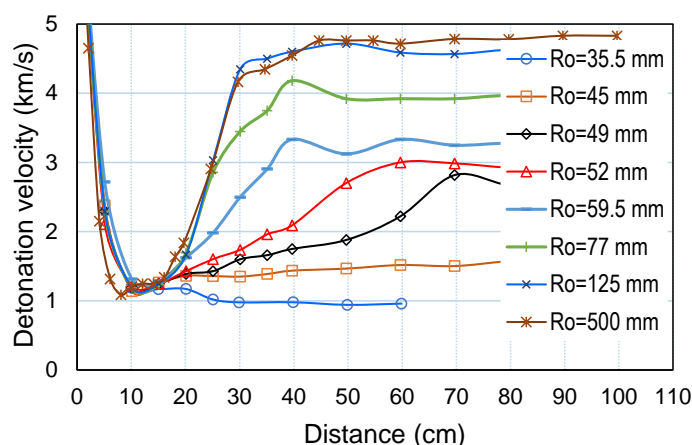

Figure 4. Calculated effect of charge diameter on VoD–x profiles.

Figure 4 shows that steady-state detonation velocity increased and was achieved at a shorter distance for larger charge radii ($x_{SDT} = 600$ mm for $R_0 = 52$ mm and $x_{SDT} = 280$ mm for $R_0 = 500$ mm). For charge radii slightly above the failure radius (31.5 mm according [37]) and 37.5 mm according to [38]), VoD growth to steady-state detonation was slower, and a steady state was attained only beyond distances of 1000 mm (Table 2 and Figure 5).

The steady-state detonation velocity as a function of charge radius was also calculated by applying the Wood–Kirkwood (WK) model incorporated into EXPLO5 thermochemical code in the way described in Section 2.2. The calculation is performed assuming light PVC confinement did not play a role, i.e., assuming the charge was unconfined. It is important to note that the WK model predicts steady-state detonation parameters, and it does not model initiation behavior. The decomposition of ANFO was described by a simple, pressure-based (PB) reaction rate model (Equation (6)) and a Lee–Tarver I&G rate model (Equation (1)). As mentioned in Section 2.2, the reaction rate constants were adjusted to reproduce our experimental detonation velocity charge radius data. Figure 6 and Table 2 show the comparison between the EXPLO5 and AUTODYN calculation results with the experimental VoD–R_0 results.
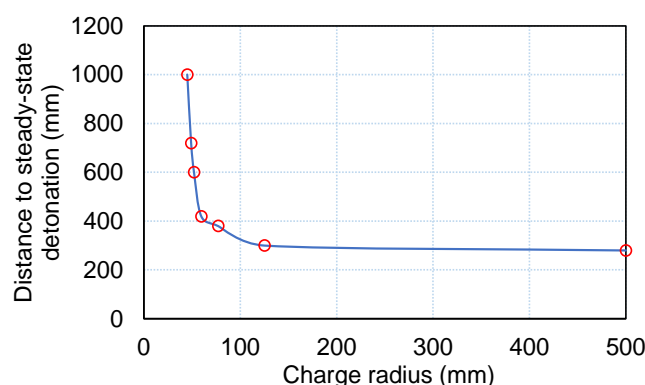

Figure 5. Dependence of run-to-steady-state detonation distance on inverse charge radius.
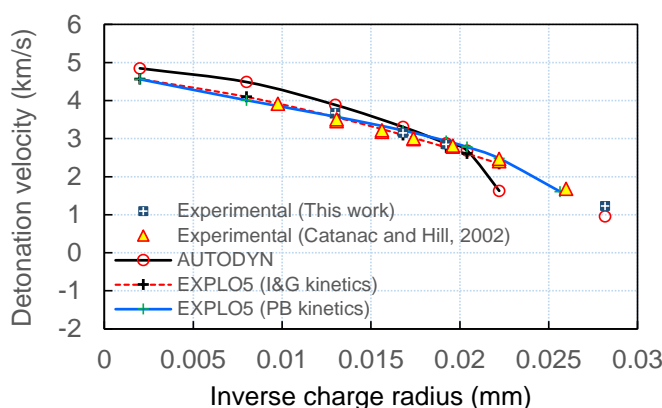

Figure 6. Comparison of experimental and calculated detonation velocity and inverse charge radii data [7].

As shown in Figure 6, both EXPLO5 and AUTODYN correctly reproduced experimental VoD–$1/R_0$ data at radii larger than 50 mm, with AUTODYN predicting slightly larger values of VoD (Table 2). The error in the predicted VoD values was larger in the vicinity of the failure radius for both the EXPLO5 and AUTODYN calculations. The pressure-based model described the experimental VoD–$1/R_0$ data very well, even in the vicinity of the failure radius, and correctly predicted the failure radius (R_f = 39 mm, which was very close to experimental value of 37.5 mm). AUTODYN and EXPLO5 with the I&G model tended to overpredict the failure radius at between 40 and 45 mm.

3.3. Effects of Booster Mass and Confinement on Shock Initiation Behavior

The effect of booster charge mass on the initiation of ANFO was studied experimentally using steel-confined charges (55 mm inner diameter, 500 mm length, and 3 mm wall thickness), and details are reported in our paper published earlier [13]. The size of the charges was kept constant in all the experiments, while the booster mass varied. The

experiments were modeled in AUTODYN using an I&G reaction rate model and the values of the I&G parameters given in Table 1. A comparative presentation of the experimental and calculated VoD–x data is given in Figure 7.
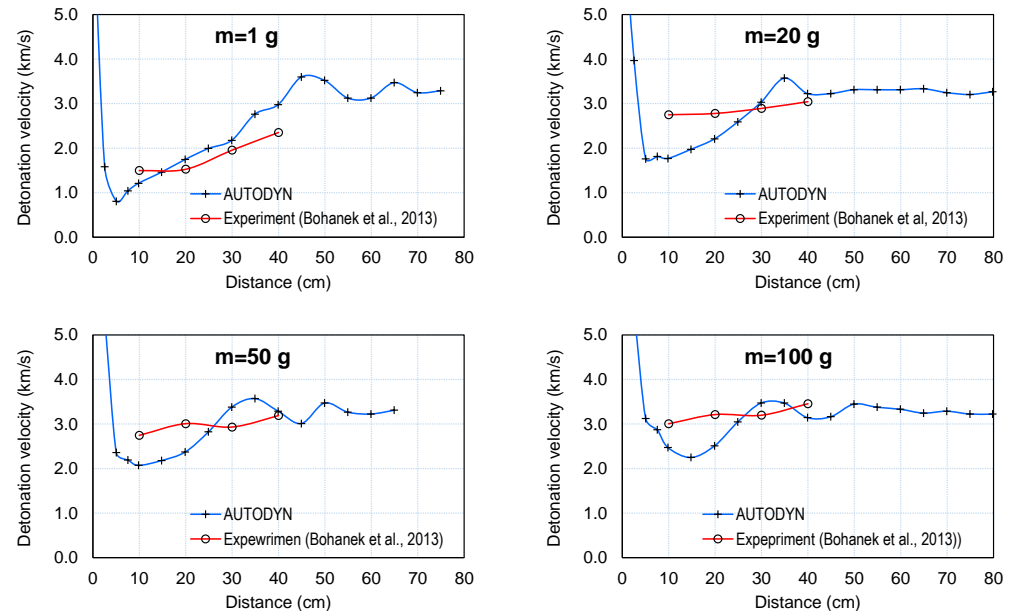

Figure 7. Experimental and calculated VoD–x profiles as a function of mass of booster for confined ANFO charges [13].

It can be seen that, similar to lightly confined ANFO charges, the calculations qualitatively described VoD–x profiles quite well. A detailed look at the comparison of the experimental results and calculations indicates that the same deficiencies of previous experiments existed. First, the small number of sections at which VoD was determined (four sections) was not sufficient to correctly register the rapid drop in shock velocity at the beginning of the charge and the existence of the minimum VoD value after which growth in shock velocity occurred. In addition, it follows from Figure 7 that the length of the explosive charges used in the experiments was not sufficient to achieve steady-state detonation in all cases. The fact that the detonation velocity determined in the last section (Section 4, x = 400 mm) was lower for charges initiated by a lower mass booster confirmed that steady-state detonation velocity was not established in all cases (because steady-state detonation velocity should be the same for the same charge size). On the contrary, the AUTODYN calculations predicted practically the same value of steady-state detonation velocity (3.32 ± 0.02 km/s), regardless of booster mass. AUTODYN calculations were performed for booster masses outside the range of the masses used in the experiments, and the results of calculations are summarized in Figure 8 and Table 3.

Table 3. Comparison of experimental and calculated detonation velocities of confined ANFO.

Booster (g)	Experiment		AUTODYN	
	VoD * (km/s)	VoD ** (km/s)	VoD_{min} (km/s)	x_{SDT} (mm)
1	2.35	3.34	0.81	450
5		3.34	1.10	400
20	3.04	3.28	1.72	330
50	3.19	3.31	2.10	320
100	3.46	3.33	2.25	290
200		3.32	2.45	260
500		3.32	2.55	250

Legend: VoD *—detonation velocity measured at section 4 (400 mm from the booster end base); VoD **—steady-state detonation velocity.

All the VoD–x curves shown in Figure 8 show a characteristic minimum, which increased and shifted to larger distances with increase in the booster mass. At the same time, the run-to-steady-state detonation distance decreased with the booster mass, while the steady-state detonation velocities remained the same (about 3.32 km/s at $x > 400$ mm). Such behavior is consistent with the findings of [2], who studied the initiation of AN/TNT mixtures with boosters of different masses.
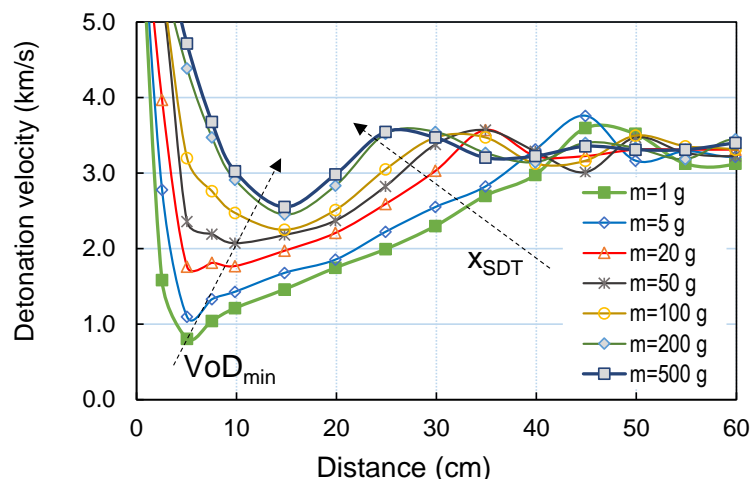

Figure 8. Calculated effect of booster mass on VoD–x curve (note: charge size is the same in all cases).

Assuming the expansion (rarefaction wave) of detonation products is similar for charges of the same size, the shape of the VoD–x curves in Figure 8 was defined primarily by reaction kinetics. A larger booster produced a larger initiating pressure impulse in the explosive region adjacent to the booster surface, resulting in a faster reaction rate (since the rate was pressure-dependent) compared to boosters of lower masses. Faster reaction, in turn, resulted in faster generation of additional pressure and energy that reinforced the initial shock wave, which led to faster growth in pressure and shock velocity and, ultimately, to a shorter distance to steady-state detonation. The fact that the rapid drop in VoD at the beginning of the charge was lower for larger boosters and that the minimum VoD shifted to larger distances with booster mass, as well as that the x_{SDT} became shorter for larger boosters, supports the aforementioned hypothesis.

The shock initiation behavior of confined and lightly confined ANFO charges is illustrated in Figure 9, which summarizes the effects of booster mass, charge diameter, and confinement on the initiation behavior of ANFO. The graph shows the dependence of x_{SDT} on booster mass in a log–log scale, and it is similar to the so-called "Pop Plot", which represents the dependence of run-to-detonation-distance on initial impact pressure [36].

As shown in Figure 9, on a log–log scale, the relationship between x_{SDT} and booster mass (m_B) data was linear. For all the charge diameters, x_{SDT} decreased with increase in the booster mass and, for $m_B = 1000$ g, x_{SDT} was approximately 250 mm, regardless of the charge radius and the existence of confinement. From the slopes of the lines, it follows that the effect of booster mass was more pronounced for smaller charge radii (slope is larger). The slope for steel-confined charges was the smallest, which indicates the smaller effect of booster mass compared to lightly confined (unconfined) charges. For illustration, the x_{SDT} for $m_B = 1000$ g equaled approximately 250 mm for all the charges. However, for $m_B = 1$ g of booster charge, $x_{SDT} = 450$ mm for the steel-confined charge of a 25.4 mm of radius, $x_{SDT} = 380$ mm for the lightly confined charge of a 77 mm radius, and $x_{SDT} = 600$ mm for the lightly confined charge of a 52 mm radius.

Such results indicated that, along with reaction rate kinetics, the expansion of detonation products plays an important role when it comes to the shock initiation of ANFO. This is the reason why, for steel-confined charges where expansion is supressed by the confining material, the x_{SDT} is much shorter than for unconfined charges, even at much

lower charge radii. Based on this, it can be expected that, with stronger confinement where radial expansion is highly supressed, the effect of booster mass on x_{SDT} may be less pronounced compared to weak confinement. It should be added that other factors (e.g., shape and size of the booster charge, position of booster charge relative to the ANFO charge, etc.) can affect, to a certain extent, the shock initiation and growth of detonation to attain a steady state.
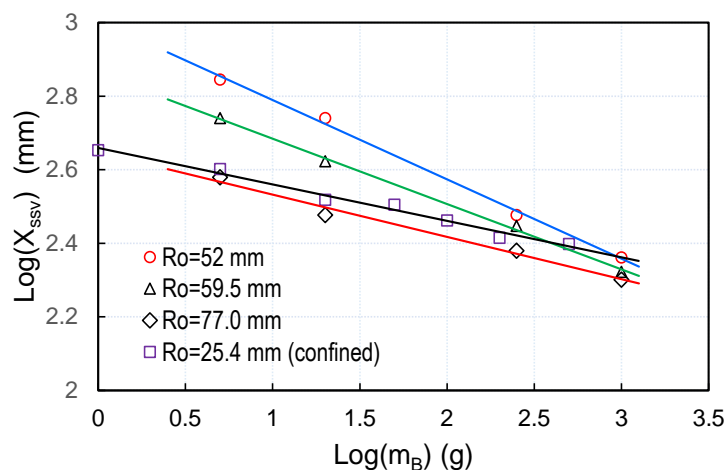

Figure 9. Summarized presentation of effects of booster mass, charge diameter, and confinement on initiation behavior of ANFO.

4. Conclusions

The shock initiation of ANFO and the effects of charge diameter, booster mass, and confinement on initiation behavior were studied experimentally by measuring detonation velocity distribution along a cylindrical explosive charge axis and were subsequently modeled using a calibrated ignition and growth (I&G) reaction rate model.

(1) It was demonstrated that AUTODYN with an I&G model could qualitatively describe the initiation process and predict steady-state detonation velocity as a function of charge diameter with an error of up to 6%. The WK detonation model incorporated into EXPLO5 thermochemical code could predict accurately the steady-state detonation velocity of unconfined (i.e., lightly confined) charges with an error of up to 3.5% for $R_0 > 50$ mm.

(2) For lightly confined charges initiated by a constant mass of booster, steady-state detonation was established faster (at shorter distances) for charges of larger diameters. The initial drop in VoD and the minimum VoD reached were related to booster mass, i.e., initiating pressure impulse, and thus did not change with charge diameter. However, the shock velocity (and pressure) growth rate increased with charge diameter. This was associated with a greater expansion of products at smaller charge diameters, which resulted in stronger pressure weakening and a slower reaction rate at smaller charge diameters. Faster reaction, in turn, resulted in faster generation of additional pressure and energy that strengthened the initial shock wave, hence leading to faster growth in pressure and shock velocity and, ultimately, to a shorter distance to steady-state detonation.

(3) Both the experiments and the calculations confirmed that booster mass strongly affected the resulting VoD–x profiles: the minimum VoD increased with booster mass and shifted to larger distances, the shock velocity growth rate increased, and the run-to-steady-state detonation decreased. On a log–log scale, x_{SDT} vs. booster mass showed linear dependence analogous to a "Pop Plot", which represents the dependence of run-to-detonation distance on initial impact pressure.

(4) The $\log(x_{SDT})$–$\log(m_B)$ graphs for lightly confined and steel-confined charges showed that the x_{SDT} was smaller for steel-confined charges, which supports the hypothesis that the expansion of detonation products plays an important role in the shock

initiation of ANFO charges. The effect of booster mass was less pronounced for steel-confined charges.

(5) Considering the wide range of parameters that could affect the shock initiation and propagation of detonation in non-ideal explosives such as ANFO, this study aimed to contribute a better understanding of the impacts of some of these factors, which is important for better tailoring the effects of ANFO for use in the mining industry.

Author Contributions: Conceptualization, M.S. and V.B.; methodology, V.B. and M.S.; software, C.H.Y.S. and B.Š.T.; validation, C.H.Y.S. and B.Š.T.; formal analysis, V.B. and M.S.; investigation; V.B. and B.Š.T.; resources V.B. and B.Š.T.; writing—original draft preparation, M.S., V.B. and C.H.Y.S.; writing—review and editing, C.H.Y.S., B.Š.T. and V.B. All authors have read and agreed to the published version of the manuscript.

Data Availability Statement: Not applicable.

Conflicts of Interest: The authors declare no conflict of interest.

References

1. Kelso, J.R.; Choromokos, J. Ammonium Nitrate/Fuel Oil Explosives. *Mil. Eng.* **1973**, *65*, 177–180.
2. Cudzilo, S.; Maranda, A.; Nowaczewski, J.; Trzciński, W.A. Shock Initiation Studies of Ammonium Nitrate Explosives. *Combust. Flame* **1995**, *102*, 64–72. [CrossRef]
3. Esen, S. A Non-Ideal Detonation Model for Commercial Explosives. Ph.D. Thesis, University of Queensland, Brisbane, QLD, Australia, 2004.
4. Fabin, M.; Jarosz, T. Improving ANFO: Effect of Additives and Ammonium Nitrate Morphology on Detonation Parameters. *Materials* **2021**, *14*, 5745. [CrossRef]
5. Cook, M.A.; Mayfield, E.B.; Partridge, W.S. Reaction Rates of Ammonium Nitrate in Detonation. *J. Phys. Chem.* **1955**, *59*, 675–680. [CrossRef]
6. King, W.A.; Bauer, A.; Heater, R.D. *The Explosion Hazards of Ammonium Nitrate and Ammonium Nitrate-Based Fertilizer Composition*; Report from Canadian Fertilizer Institue; Queen's Univeristy: Kingston, ON, Canada, 1982.
7. Catanach, R.A.; Hill, L.G. Diameter Effect Curve and Detonation Front Curvature Measurements for ANFO. In Proceedings of the AIP Conference, Albuquerque, NM, USA, 23–28 June 2002; Volume 620, pp. 906–909.
8. Sharpe, G.J.; Braithwaite, M. Steady Non-Ideal Detonations in Cylindrical Sticks of Explosives. *J. Eng. Math.* **2005**, *53*, 39–58. [CrossRef]
9. Zganec, S.; Bohanek, V.; Dobrilovic, M. Influence of a Primer on the Velocity of Detonation of ANFO and Heavy ANFO Blends. *Cent. Eur. J. Energ. Mater.* **2016**, *13*, 664–704. [CrossRef]
10. Miyake, A.; Takahara, K.; Ogawa, T.; Ogata, Y.; Wada, Y.; Arai, H. Influence of Physical Properties of Ammonium Nitrate on the Detonation Behaviour of ANFO. *J. Loss Prev. Process Ind.* **2001**, *14*, 533–538. [CrossRef]
11. Zygmunt, B.; Buczkowski, D. Influence of Ammonium Nitrate Prills' Properties on Detonation Velocity of ANFO. *Propellants Explos. Pyrotech.* **2007**, *32*, 411–414. [CrossRef]
12. Buczkowski, D.; Zygmunt, B. Influence of Ammonium Nitrate Prills Porosity and Dimensions on Detonation Velocity of ANFO Explosives. In Proceedings of the New Trends in Research of Energetic Materials, Pardubice, Czech Republic, 21–23 April 2003; pp. 45–51.
13. Bohanek, V.; Dobrilović, M.; Škrlec, V. Influence of the Initiation Energy on the Velocity of Detonation of ANFO Explosive. *Cent. Eur. J. Energ. Mater.* **2013**, *10*, 555–568.
14. Dobrilovic, M.; Bohanek, V.; Zganec, S. Influence of Explosive Charge Temperature on the Velocity of Detonation of ANFO Explosives. *Cent. Eur. J. Energ. Mater.* **2014**, *11*, 191–197.
15. Zygmunt, B.; Buczkowski, D. Agriculture Grade Ammonium Nitrate as the Basic Ingredient of Massive Explosive Charges. *Propellants Explos. Pyrotech.* **2012**, *35*, 685–690. [CrossRef]
16. Jackson, S.I.; Kiyanda, C.B.; Short, M. Precursor Detonation Wave Development in ANFO Due to Aluminum Confinement. In Proceedings of the 14th International Detonation Symposium, Coeur D'Alene, ID, USA, 11–16 April 2010; pp. 740–749.
17. Bohanek, V.; Sućeska, M.; Dobrilović, M.; Hartlieb, P. Effect of Confinement on Detonation Velocity and Plate Dent Test Results for ANFO Explosive. *Energies* **2022**, *15*, 4404. [CrossRef]
18. van der Steen, A.C.; Kodde, H.H.; Miyake, A. Detonation Velocities of the Non-Ideal Explosive Ammonium Nitrate. *Propellants Explos. Pyrotech.* **1990**, *15*, 58–61. [CrossRef]
19. Suceska, M. *EXPLO5 Version V6.05 Users' Guide*; OZM Research: Hrochuv Tynec, Czech Republic, 2018.

20. Wood, W.W.; Kirkwood, J.G. Diameter Effect in Condensed Explosives. the Relation between Velocity and Radius of Curvature of the Detonation Wave. *J. Chem. Phys.* **1954**, *22*, 1920–1924. [CrossRef]

21. Kirby, I.J.; Leiper, G.A. A Small Divergent Detonation Theory for Intermolecular Explosives. In Proceedings of the 8th International Detonation Symposium, Albuquerque, NM, USA, 15–19 July 1985; pp. 176–186.

22. Lee, E.L.; Tarver, C.M. Phenomenological Model of Shock Initiation in Heterogeneous Explosives. *Phys. Fluids* **1980**, *23*, 2362–2372. [CrossRef]

23. Kittell, D.E.; Cummock, N.R.; Son, S.F. Reactive Flow Modeling of Small Scale Detonation Failure Experiments for a Baseline Non-Ideal Explosive. *J. Appl. Phys.* **2016**, *120*, 064901. [CrossRef]

24. Stimac, B.; Skrlec, V.; Dobrilovic, M.; Suceska, M. Numerical Modelling of Non-Ideal Detonation in ANFO Explosives Applying Wood-Kirkwood Theory Coupled with EXPLO5 Thermochemical Code. *Def. Technol.* **2020**, *17*, 1740–1752. [CrossRef]

25. Fried, L.E.; Howard, W.M.; Souers, P.C.; Haselman, L. *Adding Kinetics and Hydrodynamics to the CHEETAH Thermochemical Code*; Report No. UCRL-ID-125794; Lawrence Livermore National Laboratory: Livermore, CA, USA, 1997.

26. Esen, S.; Souers, P.C.; Vitello, P. Prediction of the Non-Ideal Detonation Performance of Commercial Explosives Using the DeNE and JWL++codes. *Int. J. Numer. Methods Eng.* **2005**, *64*, 1889–1914. [CrossRef]

27. ANSYS Inc. *ANSYS Autodyn: User's Manual Release 13.0*; ANSYS Inc.: Canonsburg, PA, USA, 2010.

28. Yi, C.; Nyberg, U.; Johansson, D. Calibration and Validation of Reactive Flow Model Parameters for an Emulsion Explosive. In Proceedings of the FragBlast 12: 12th International Symposium on Rock Fragmentation by Blasting, Lulea, Swedan, 11–13 June 2018; pp. 459–468.

29. Li, Y.; Yang, X.; Wen, Y.; Xiong, S.; Li, X. Determination of Lee-Tarver Model Parameters of JO-11C Explosive. *Propellants Explos. Pyrotech.* **2018**, *43*, 1032–1040. [CrossRef]

30. Fickett, W.; Davis, W.C. *Detonation Theory and Experiment*; Dover Publications, Inc.: Mineola, NY, USA, 2000.

31. Fried, L.E.; Souers, P.C. BKWC: An Empirical BKW Parametrization Based on Cylinder Test Data. *Propellants Explos. Pyrotech.* **1996**, *21*, 215–223. [CrossRef]

32. Souers, P.C.; Anderson, S.; Mercer, J.; McGuire, E.; Vitello, P. JWL++: A Simple Reactive Flow Code Package for Detonation. *Propellants Explos. Pyrotech.* **2000**, *25*, 54–58. [CrossRef]

33. Braithwaite, M.; Cunningham, C.V.B.; Sharpe, G.J. Modeling and Numerical Simulation of Steady State Detonations in Highly Non-Ideal Explosives. In Proceedings of the 13th International Detonation Symposium, Norfolk, VA, USA, 23–28 July 2006.

34. Suceska, M.; Stimac Tumara, B.; Dobrilovic, M.; Bohanek, V. Estimation of Detonation Front Curvature Radius by Empirical Equations. *J. Energ. Mater.* **2022**, 1–18. [CrossRef]

35. Fried, L.E.; Howard, W.M.; Souers, P.C. *Cheetah 2.0 User's Manual*; Lawrence Livermore National Laboratory: Livermore, CA, USA, 1998.

36. Urtiew, P.A.; Vandersall, K.S.; Craig, M.; Garcia, F.; Forbes, J.W. Shock Initiation Experiments and Modeling of Composition B and C-4. In Proceedings of the 13th International Detonation Symposium, Norfolk, VA, USA, 23–28 July 2006; pp. 929–939.

37. Souers, P.C.; Vitello, P. *ANFO Calculations for Sedat Esen*; Lawrence Livermore National Lab. (LLNL): Livermore, CA, USA, 2004.

38. Jackson, S.I.; Short, M. Scaling of Detonation Velocity in Cylinder and Slab Geometries for Ideal, Insensitive and Non-Ideal Explosives. *J. Fluid Mech.* **2015**, *773*, 224–266. [CrossRef]